J Mater Sci (2009) 44:5127–5142
DOI 10.1007/s10853-009-3635-0

FERROELECTRICS

Dynamic magneto-electric multiferroics PZT/CFO multilayered nanostructure

N. Ortega · Ashok Kumar · Ram S. Katiyar · Carlos Rinaldi

Received: 30 March 2009 / Accepted: 21 May 2009 / Published online: 19 June 2009

Abstract Highly oriented $PbZr_{0.53}Ti_{0.47}O_3/CoFe_2O_4$(PZT/CFO) multilayered nanostructures (MLNs) were grown on MgO substrate by pulsed laser ablation using $La_{0.5}Sr_{0.5}CoO_3$ (LSCO) as conducting bottom electrode. The effect of various PZT/CFO (PC) sandwich configurations having three, five, and nine layers while maintaining total thickness of PZT and CFO be identical has been systematically investigated. X-ray diffraction (XRD) and micro-Raman spectra revealed the existence of pure PZT and CFO phases without any intermediate phase. Intact MLNs were observed by transmission electron microscopy (TEM) with little inter-diffusion near the interfaces at nano-metric scale without any impurity phase. Impedance spectroscopy, modulus spectroscopy, and conductivity spectroscopy were carry out over a wide range of temperatures (100–600 K) and frequencies (100 Hz–1 MHz) to investigate the grain and grain boundary effect on electrical properties of MLNs. Temperature dependent real dielectric permittivity and dielectric loss illustrated step-like behavior and relaxation peaks near the step-up characteristic, respectively. Cole–Cole plots indicate that most of the dielectric response came from the bulk (grain) MLNs below 300 K, whereas the grain boundary and the electrode–MLNs effects are prominent at elevated temperatures. The dielectric loss relaxation peak shifted to higher frequency side with increase in temperature, it was out of the experimental frequency window above 300 K. Our Cole–Cole fitting of dielectric loss spectra indicated marked deviation from the ideal Debye-type of relaxation, which is more at elevated temperature. Master modulus spectra supported the observation from the impedance spectra; it also indicated that the magnitude of the grain boundary compared to grain becomes more prominent with increase in number of layers. We have explained these electrical properties of MLNs by Maxwell–Wagner type contributions arising from the interfacial charge at the interface of the ML structures. Three different types of frequency dependent conduction processes were observed at elevated temperatures (>300 K), which fitted well with the double power law, $\sigma(\omega) = \sigma(0) + A_1\omega^{n_1} + A_2\omega^{n_2}$, indicating that the low frequency (<1 kHz) conductivity may be due to long-range ordering (frequency independent), mid frequency conductivity (<10 kHz) may be due to short-range hopping, and high frequency (<1 MHz) conduction due to the localized relaxation hopping mechanism. Ferroelectric polarization decreased slowly in reducing the temperature from 300 to 200 K, with complete collapse of polarization at $\sim$100 K, but there was complete recovery of the polarization during heating, which was repeatable over many different experiments. At the same time, the temperature dependent remanent magnetization of the MLNs showed slow enhancement in the magnitude till 200 K with three-fold increase at 100 K compared to room temperature. This enhancement in remanent magnetization and decrease in remanent ferroelectric polarization on lowering the temperature indicate temperature dependent dynamic switching of ferroelectric polarization. The magnetic and ferroelectric

N. Ortega · A. Kumar · R. S. Katiyar (✉)
Department of Physics and Institute for Functional Nanomaterials, University of Puerto Rico, San Juan, PR 00931-3343, USA
e-mail: rkatiyar@hpcf.upr.edu

A. Kumar
e-mail: Ashok553@gmail.com

C. Rinaldi
Department of Chemical Engineering and Institute for Functional Nanomaterials, University of Puerto Rico, Mayagüez, PR 00681-9046, USA

properties of MLNs were quite different compared to individual layers suggesting its improper ferroelectric characteristics. The fatigue test showed almost 0–20% deterioration in polarization. Fatigue and strong temperature and frequency dependent magneto-electric coupling suggest MLNs utility for Dynamic Magneto-Electric Random Access Memory (DMERAM).

Introduction

Magneto-electric (ME) multiferroic materials are of tremendous technological and scientific interest due to their ME properties originating from the coupling between various ordered parameters, i.e., ferro-electric, ferro-elastic, and ferro-magnetic. The interplay among these parameters allows magnetic control of ferroelectricity/polarization, electric control of magnetization, control of magnetism with stress, and could yield new device concepts, such as multiferroic tunnel junction, ME random access memory, etc. [1–4]. Recently, with the advancement of ultrathin film growth technique, it is possible to fabricate artificial multiferroics at nanoscale with help of alternate layers of ferroelectric and ferromagnetic materials [5]. The MLNs multiferroics may play important role in future ME devices because none of the existing single phase multiferroic compounds have large and robust ferroelectric and ferromagnetic polarizations at room temperature [6, 7]. Theoretically and experimentally it has been proved that layered structure or composites have very high ME coupling compared to single phase materials, but at the same, it showed very slow switching mechanism, which hindered its applications in memory devices [8–10]. There are several ways to fabricate artificial ME multiferroics, among them composites, layered structures, and vertically aligned nanostructures are of considerable interest [7, 9, 11]. The basic mechanism behind ME coupling in these nano-structures is electrostrictive, i.e., elastic components of ferroelectric and ferromagnetic coupled trough strain. Recently, it has been found that ME coupling in MLNs may also occur due to interface bonding [12, 13]. Displacements of atoms at the interface caused by ferroelectric instability alter the overlap between atomic orbitals at the interface thus affecting the interface magnetization. ME composite thin films with different configurations were reported in literature, such as double $Pb(Zr,Ti)O_3$ (PZT)/$CoFe_2O_4$ (CFO) multilayers [14], superlattices consisting of alternating FM ($Pr_{0.88}Ca_{0.15}MnO_3$), and FE ($Ba_{0.6}Sr_{0.4}TiO_3$) layers deposited on $SrTiO_3$ [15], epitaxial $CoFe_2O_4$–$BaTiO_3$ ferro-electromagnetic nanocomposites by self assembly technique [7], etc. Our prior report showed the ME effect in PZT/CFO multilayer composite thin films [16].

A powerful and versatile complex impedance spectroscopy technique has been used to analyze the microstructure–property relationship; it also allows distinguishing between intrinsic (bulk) and extrinsic contributions (grain boundary, surface layer, and electrode contact problem). An equivalent circuit based on impedance and modulus spectra provides the physical process occurring inside the sample. Impedance spectroscopic studies of ferro-electromagnetic ceramic $Pb(Fe_{1/2}Nb_{1/2})O_3$, ME polycrystalline samples $Bi_6Fe_2Ti_3O_{12}$, and PZT/CFO MLNs with polycrystalline nature has been carried out, which described the connection between microstructure and electrical properties in terms of brick-layer model and parallel resistance (R), capacitance (C) circuit [17–19]. The electrical and dielectric behavior of $ACu_3Ti_4O_{12}$ (A = Ca, $Bi_{2/3}$, $Y_{2/3}$, $La_{2/3}$) [20, 21] ceramic samples are discussed with the help of impedance spectroscopy. These structures exhibit a Debye-like relaxation (Maxwell–Wagner type) and their dielectric constant is nearly independent of frequency and temperature. Catalan et al. did an extensive study on the Maxwell–Wagner space charge effects in superlattice structure [22–24]. We have also explained the Maxwell–Wagner charge effects in PZT/CFO polycrystalline MLNs structures [25].

Recently, we discovered the dynamic temperature dependent ME coupling in highly oriented PZT/CFO MLNs and explained this phenomena based on several prior experimental observations, such as internal barrier layer capacitors (IBLC) [21, 26] defect-induced polarizations, domain pinning (freezing domain) [27], improper ferroelectricity [28], and ME effects based on structural phase transitions [29]. Our previous studies have demonstrated biferroic and ME properties of these materials in different configurations [16, 19, 25]. As we know, a large ME effect in thin film nanostructures is needed for useful device applications, i.e., modulators, generators, sensors, and memories. However, the temperature and frequency dependent fundamental physics of these MLNs needs to be understood for proper applications in devices.

In the present paper, we studied dielectric, polarization, magnetization, impedance, modulus, and AC conductivity as a function of the temperature (100–650 K) and frequency (10^2–10^6 Hz) of the epitaxial PZT/CFO MLNs with three, five, and nine layers fabricated on $La_{0.5}Sr_{0.5}CoO_3$ (LSCO) coated (001) MgO (LM) substrates using the pulsed laser deposition technique. The goal of this investigation is to improve our understanding of the PZT/CFO MLNs thin film properties by analyzing the electrical response of the grain and grain boundary effects. A correlation of the electric conduction process and their interpretation in terms of microscopic process has been carried out for the different configurations of the PZT/CFO MLNs. Ferroelectric and ferromagnetic properties at room

temperature and their ME coupling is well established. The temperature and frequency dependence of the effect of ferromagnetic layers on the ferroelectric and electrical properties and vice versa remain to be explored. These effects are fundamental to technological applications. The effect of frequency and temperature on the remanent polarization of MLNs thin films will be discussed in terms of dynamic temperature dependent enhancement of remanent magnetization.

Experimental

Multilayered nanostructures (MLNs) of thin films with three (L3), five (L5), and nine (L9) alternating layers of PZT/CFO were fabricated on conducting (bottom electrode) $La_{0.5}Sr_{0.5}CoO_3$ (LSCO) coated (100) MgO substrate using pulse laser deposition by individual PZT and CFO targets. PZT and CFO ceramic targets of 2 cm diameter were prepared by conventional solid-state route. An excimer laser (KrF, 248 nm) with a laser energy density of 1.5 J/cm^2 and pulse repetition rate of 10 Hz was used to deposit ML films. The substrate temperature was maintained at 400 °C with oxygen pressure of 100 mTorr during the deposition. The deposited films were annealed at 700 °C for 150 s using a rapid thermal annealing (RTA) furnace. The phase purity of films were characterized by X-ray diffraction (XRD) using Cu K_α radiation in a Siemens D500 diffractometer, and the thickness ($\sim$350 nm) of layered structure by transmission electron microscopy (TEM) using an FEI Tecnaic F20 at operating energy $\sim$200 kV. For electrical measurements, capacitors were fabricated by sputtering Pt top electrodes with a diameter of $\sim$200 μm through a shadow mask. The temperature dependent impedance, conductance, real part of dielectric constant and dielectric losses were measured in the frequency range of 10^2 to 10^6 Hz and temperatures from 100 to 650 K using an HP4294 impedance analyzer. The temperature was controlled with an accuracy of ±0.5 °C using a temperature controller (K-20 MMR technologies INC). Magnetic measurements were carried out using a Quantum Design MPMS XL-7 SQUID magnetometer. The sample was placed in a standard drinking straw sample holder and the sample space was evacuated multiple times to ensure removal of air by displacing it with He. To find the remanent magnetization, zero field cooled/field cooled (ZFC/FC) measurements were made by first warming the sample to 400 K under zero field, then cooling to 2 K and applying the target magnetic field at that temperature. The samples were then warmed to 400 K, obtaining the ZFC data, and again cooled to 2 K, obtaining the FC data. After the ZFC/FC measurements were made, hysteresis curves were measured from 4 to 400 K under applied fields of up to 7 T. Magnetic measurements were carried out parallel to the *c*-axis (i.e., applied field was perpendicular to the substrate).

Results and discussion

MLNs crystal structure and microstructure

Room temperature XRD pattern of L5 MLNs are shown in Fig. 1a. The XRD patterns indicate highly oriented films, with diffraction peaks of perovskite PZT along (001) orientation and spinel CFO along (004) (overlapping with MgO substrate peaks). The observation of distinct peaks for PZT and CFO without the appearance of any additional peak suggested that individual ferroelectric and ferromagnetic phases were retained in the ML structure. Room temperature micro-Raman spectra of L5 MLNs are shown in inset of Fig. 1a. All of the Raman active peaks can be easily assigned by individual PZT and CFO peaks. No extra peaks were observed that indicates the absence of

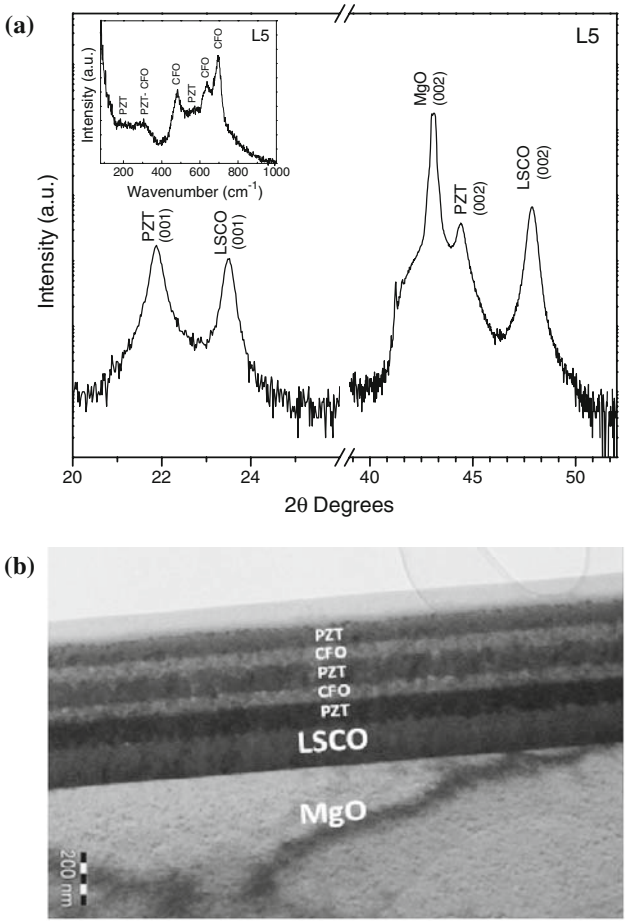

Fig. 1 Room temperature **a** X-ray diffraction pattern and Raman spectra (inset) and **b** cross-sectional TEM image of five-layers (L5) thin film, grown on LSCO-coated (100) MgO substrate

intermediate phase in MLNs. Similar results were obtained for L3 and L9 MLN thin films.

Lattice mismatch strain (ε) between the substrate and the first layer and intermediate layers were analyzed on the basis of the inplane epitaxial relationship MLs [100] || LSCO [100] || MgO [100], we calculate the lattice mismatch using the following equation:

$$\varepsilon = \frac{a_{\text{sub}} - a_{\text{film}}}{a_{\text{sub}}} \times 100, \tag{1}$$

where (ε) is the lattice mismatch, a_{sub} is the lattice constant of the substrate or intermediate layer and, a_{film} is the lattice constant of the PZT. We observed a tensile strain ($\sim$4.20% along a-axis, 1.59% along c-axis) between substrate/MLNs and compressive strain ($\sim -5.24\%$ along a-axis, -8.10% along c-axis) between bottom electrode/MLNs. Strain across the interfaces of PZT/CFO were examined, which revealed that a compressive strain of $\sim -3.96\%$ along a-axis, -1.21% along c-axis. The calculated comparative strains at the interfaces of parent layer along a-axis and c-axis are very high that generate a high electro-striction across the interfaces, which may one of the reason for dynamic ME coupling. Figure 1b illustrated the cross-sectional TEM images of L5 MLNs. TEM of L5 MLNs thin film revealed a multilayer structure with well-defined and distinctly ferromagnetic (CFO) and ferroelectric (PZT) layers and also that the film thickness of each layers are uniform over a region of several micrometers. TEM picture also showed good interfaces between different layers, indicating that the CFO layers were well distinct from the PZT layers. The scanning transmission electron microscopy (STEM) line scan across the L5 MLNs (not shown here), suggests uniform distribution of ferroelectric and ferrimagnetic layers near the interface, with little inter-diffusion of pure PZT and pure CFO almost nano-metric scale near the interface. XRD, Raman spectra, and micro-structural results suggest that uniform MLNs with different configurations were formed having high orientation (001), little inter-diffusion near the interfaces, no extra phase respect to parent layers, and high in-plane and out of plane strain across PZT and CFO layers.

Dielectric spectroscopy

Figure 2a, b show Cole–Cole plots and frequency dispersion of imaginary (ε'') parts of the permittivity, respectively, over 100 Hz–1 MHz for all L3, L5, and L9 MLNs at different temperatures. The values of ε' and ε'' were obtained using

$$\varepsilon^* = \varepsilon' - i\varepsilon'' = \frac{1}{i\omega C_0 Z^*}, \tag{2}$$

where ω is the angular frequency $\omega = 2\pi f$, and $i = \sqrt{-1}$, $C_0 = \varepsilon_0 A/d$ the empty cell capacitance, A the sample area, and d the sample thickness. The Cole–Cole plots and frequency dependence of the dielectric relaxation can be represented by the empirical Cole–Cole relaxation [30]:

$$\varepsilon^*(\omega) = \varepsilon'(\omega) - i\varepsilon(\omega) = \varepsilon_\infty + \frac{(\varepsilon_0 - \varepsilon_\infty)}{1 + (i\omega\tau_0)^{1-\alpha}}, \tag{3}$$

where ω is frequency of the applied electric field (10^2–10^6 Hz), ε_0 and ε_∞ the static and high-frequency limit of the dielectric constant, τ_0 the most probable relaxation time, and α a constant with values between 0 and 1; for $\alpha = 0$, Eq. 3 reduces to the Debye expression, $\alpha > 0$ implies that there is a relaxation time distribution, leading to a peak shape broader than Debye. The Cole–Cole plot (Fig. 2a) showed almost bulk permittivity (single semicircle) of MLNs from 200 to 350 K, above 400 K extrinsic contributions take into effect in the experimental frequency window, which may be due to the grain boundary permittivity, local permittivity near the interface of different layers and MLNs–electrode space charge at elevated temperature. Values of bulk permittivity of MLNs decreases with increase in number of layers from L3 to L9. The nature of semicircle is more depressed with increase in number of layers, which in turns increase the value of constant α from 0.29 to 0.44 suggesting higher order of dispersiveness (poly) in L9 compare to L3. Extrinsic contributions dominated in MLNs above 450 K.

Our Cole–Cole fitting of dielectric loss spectra (*solid lines* in Fig. 2b) indicated marked deviation from Debye-type. The values of α lie between 0.29 and 0.44 (see Table 1) for different MLNs at different frequencies, indicating polydispersive MLs; and this dispersion increases with temperature and number of layers. The literature survey revealed that the PZT multilayer structures have $\alpha = 0.51$ very near to our higher configuration L9 MLNs values [31]. The inverse peak frequency follows Arrhenius law

$$\tau = \tau_0 \exp(-E_a/k_B T) \text{ where } \tau = 1/2\pi f_p \tag{4}$$

where τ_0 is the prefactor, E_a the activation energy for the relaxation process, and k_B the Boltzman constant. The activation energy associate with this process ranging from 0.38 to 0.44 eV for different MLNs, the details are given in Table 1. The value of activation energy increases with layer numbers. This activation energy (E_a) corresponds to the activation energy of electronic contribution calculated for multiferroic materials [31]. The increase in E_a with increase in MLNs implies a decrease in space–charge mobility in agreement with mobilities calculated (10^{-10} cm^2/Vs) for PZT multilayers by Jiang et al. [32]. The relaxation peaks of dielectric loss spectra shifted to lower frequencies with decreasing temperature; below 200 K, they moved out of our measurable frequency range. Detailed analysis indicated a non-Debye-type (polydispersive) relaxation in MLs

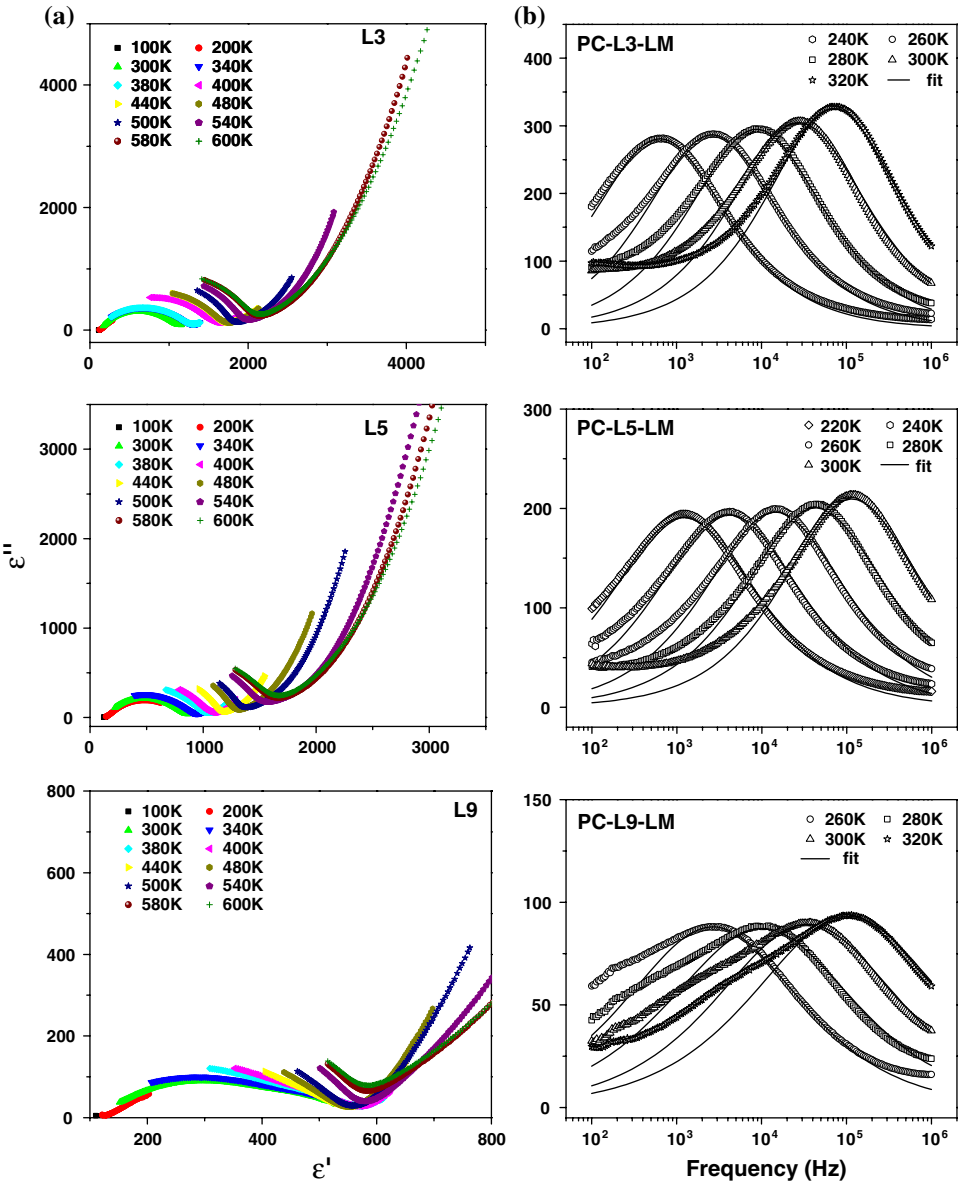

Fig. 2 **a** Complex permittivity plane plot ε' versus ε'' and **b** frequency dependence of the imaginary (ε'') part of the permittivity, the Cole–Cole equation fits as shown as continuous lines, for L3, L5, and L9 multilayer structures at different temperatures

Table 1 Activation energy E_a and average of exponential parameter $\overline{\alpha}$ constant determined by fitting the ε'' versus f data for each MLN structure

Multilayer thin films	E_a (eV)	$\overline{\alpha}$
PC-L3-LM	0.38	0.29
PC-L5-LM	0.33	0.32
PC-L9-LM	0.44	0.44

structure, transforming to Debye-type (monodispersive) relaxation on lowering the temperature below 200 K.

Impedance spectroscopy

Figure 3a, b shows the variation of imaginary part of impedance (Z'') as a function of frequency at low and high temperature, respectively. The peaks showed in Fig. 3a correspond to the grain contribution; these peaks are very faint, to come at any conclusions based on these data are very difficult. To see the real effect of grain contribution, later, we have analyzed our data based on master modulus spectroscopy. However, the grain contribution in all of the MLNs can be easily seen from Fig. 3b at high temperature, similarly to polycrystalline films [19], peak maxima were observed with shifts systematically toward higher frequencies on increasing the temperature. The intensity of Z'' peak was varying strongly with temperature, indicating Arrhenius-type temperature dependence. The activation energy associated with the grain boundary relaxation process was determined using Arrhenius equation. The grain boundary activation energy (E_{gb}) values of highly oriented L3, L5, and L9 MLNs were listed the Table 2. That means,

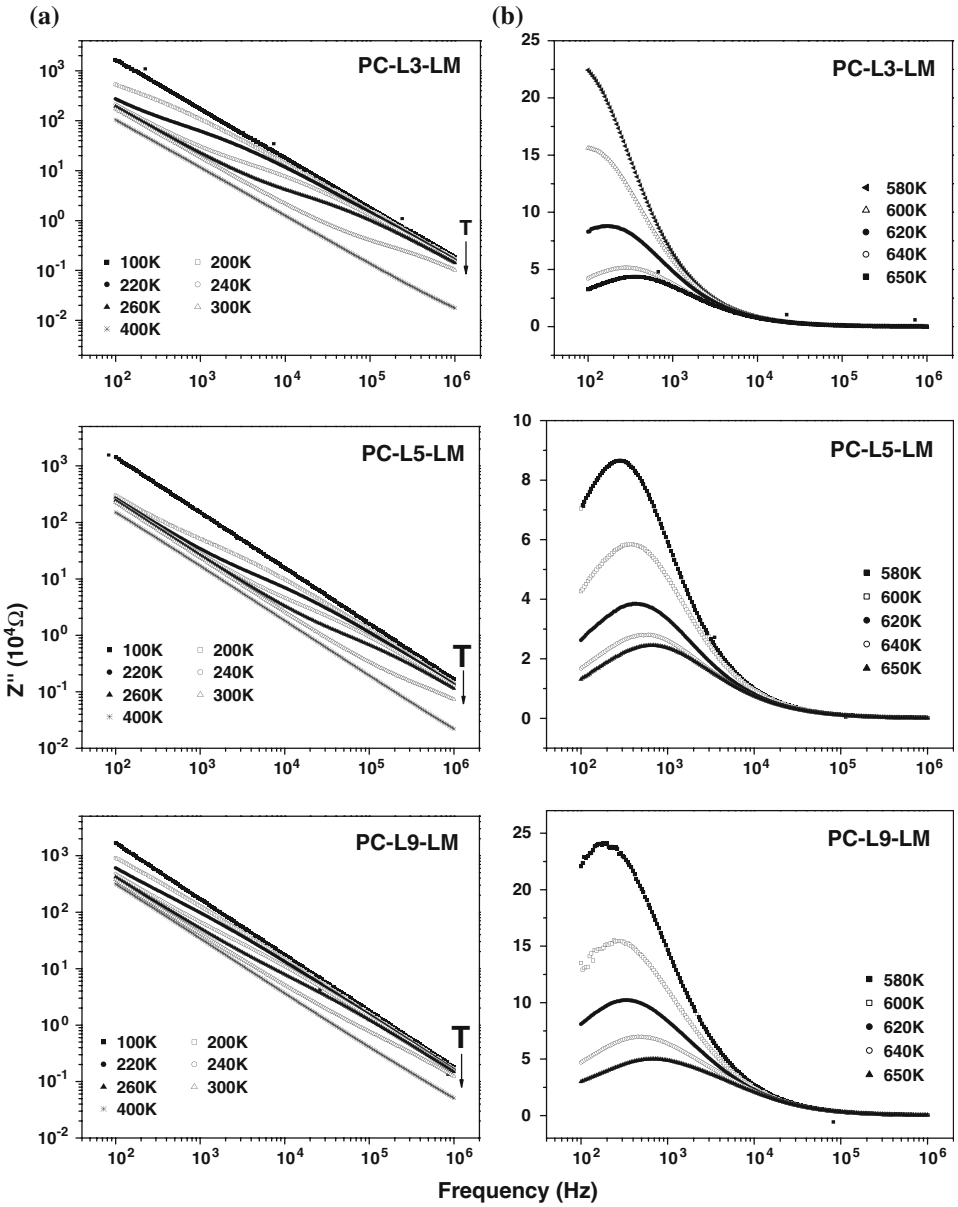

Fig. 3 Frequency dependence of imaginary part of impedance spectra Z'': **a** at low temperature, frequency response peaks are mainly due to grain effect, and **b** at elevated temperature (>550 K), low frequency response peaks are mainly due to grain boundary effects at different temperatures for PZT/CFO high-oriented multilayer structures

Table 2 Activation energies and prefactors the grain (E_g, τ_{0g}) and grain boundary (E_{gb}, τ_{0gb}) relaxation process of MLN thin films determined by fitting the M'' data and average of stretched exponential parameter (β) for each ML structure. E'_{gb} was calculated from Z'' versus f

Thin films	E'_{gb} (eV)	E_g (eV)	E_{gb} (eV)	τ_g (s)	τ_{gb} (s)	β_g	β_{gb}
PC-L3-LM	0.45	0.410	1.004	$10^{-12.84}$	$10^{-12.82}$	0.475	0.484
PC-L5-LM	1.04	0.272	0.805	$10^{-10.57}$	$10^{-9.96}$	0.464	0.520
PC-L9-LM	0.99	0.425	0.986	$10^{-12.82}$	$10^{-11.68}$	0.432	0.451

the effects of numbers of interfaces between layers, grain size, and grain boundary play an important role in the electrical properties of the ML thin films, even in highly oriented ML thin films. The value of grain boundary activation energy becomes perturbed with increase in the number of layers. This indicates more energy requires for the mobility of charge carriers through grain boundary in L5 and L9 ML structure.

Figure 4 shows the complex plot between the real and imaginary components of the impedance of highly oriented

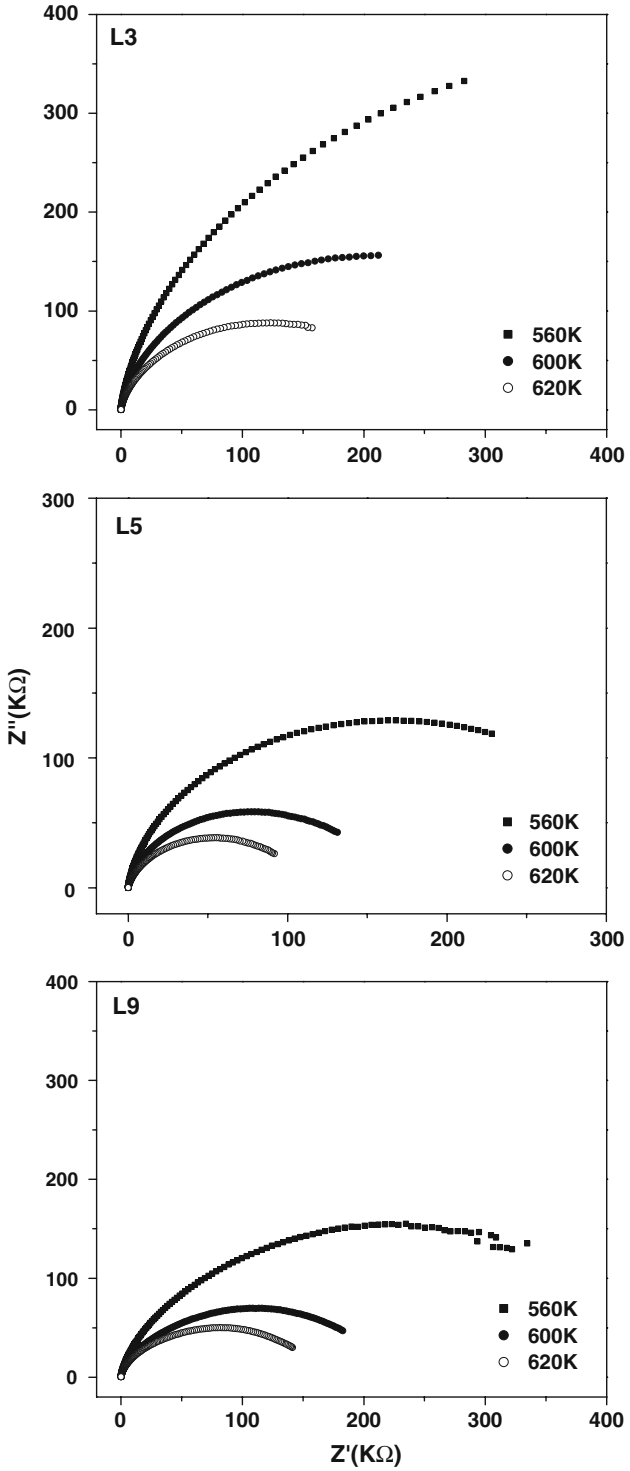

Fig. 4 Complex impedance plane plot (Z'' versus Z') for PZT/CFO high-oriented MLs thin films at high temperatures (≥560)

L3, L5, and L9 MLNs thin films at various temperatures, in the 100 Hz–1 MHz frequency range. All the semicircles became smaller with increase in temperature and shifted toward the lower Z' values, indicating a reduction in the resistance. In the entire temperature range, the center of the semicircles lies below the real axis, suggesting a non-Debye response.

To analyze the impedance data, it is usually modeled by an ideal equivalent electrical circuit comprising of resistance (R) and capacitance (C). The equivalent circuit is based on the brick-layer model [19]. We ignore the parallel channel of grain boundary resistance and capacitance. These highly oriented MLNs show that grain and grain boundary impedance can be represented by equivalent circuit consisting of a series combination of grain and grain boundary elements. The grain circuit consists of a parallel combination of grain resistance (R_g) and grain capacitance (C_g), whereas as the grain boundary consists of parallel combination of grain boundary resistance (R_{gb}) and grain boundary capacitance (C_{gb}). The equivalent electrical equation can be represented as follows:

$$Z^* = Z' - jZ'' = \frac{1}{R_g^{-1} + j\omega C_g} + \frac{1}{R_{gb}^{-1} + j\omega C_{gb}}, \tag{5}$$

$$Z' = \frac{R_g}{1 + \left(\omega R_g C_g\right)^2} + \frac{R_{gb}}{1 + \left(\omega R_{gb} C_{gb}\right)^2}, \tag{6}$$

$$Z'' = R_g\left(\frac{\omega R_g C_g}{1 + \left(\omega R_g C_g\right)^2}\right) + R_{gb}\left(\frac{\omega R_{gb} C_{gb}}{1 + \left(\omega R_{gb} C_{gb}\right)^2}\right), \tag{7}$$

$$Z'' = R_{gb}\left(\frac{\omega R_{gb} C_{gb}}{1 + \left(\omega R_{gb} C_{gb}\right)^2}\right). \tag{8}$$

As shown in Fig. 4a, the impedance loss peaks attributed to the grains, are so weak that we cannot analyze data by Eq. 7. At elevated temperature (>400 K), strong impedance loss peak attributed to the grain boundary in the low frequency side appears in the experimental frequency window while grain peaks already moved out. Hence, the magnitude of impedance loss (Z'') can be fitted by an equivalent circuit consisting of parallel combination of C_{gb} and R_{gb} that can be represented by Eq. 8.

The Cole–Cole equation, which is commonly used for polycrystalline materials, is given below:

$$Z^* = \frac{R_{gb}}{R_{gb} + (j\omega\tau)^{\alpha}} \tag{9}$$

where τ is the relaxation time and $\alpha(0 < \alpha \leq 1)$ is the parameter to calculate the deviation from ideal Debye-type relaxation. We fitted our data with Debye model; we observed that the response from the grain boundary is not following the ideal Debye relaxation. The full width at half maxima (FWHM) calculated from the impedance loss spectra are greater than 1.141 decade (ideal Debye relaxation) indicating a deviation from the Debye-type relaxation. It can be seen that the number of individual PZT and CFO layers increases from L3 to L9 configuration, which

increases the number of interfaces, and at the same time, there is higher order of inter-diffusion between the two layers. The enhancement of inter-diffusion provides more grain boundary contributions in L9 MLNs. In the present investigation, it can be observed that if a layered nanostructure has more number of layers and low profile sharp interface that gives more grain boundary path, which acts like short circuit for conduction mobile charge carriers, which drastically reduces the grain boundary resistance.

Modulus spectroscopy

The complex modulus plots of L3, L5, and L9 MLNs are shown in Fig. 5. The data indicate the presence of two well-resolved semicircles: the first semicircle represents the capacitive grain boundary effects at elevated temperatures and the second one to the capacitive grains effects in low temperature regions [33, 34]. The electric modulus spectroscopy is a powerful tool to investigate low capacitive effects, since these MLNs showed very weak grain effects in impedance loss spectra compared to grain boundary effects. The electric modulus magnifies the grain capacitive effects making them easier to analyze. To analyze the grain effects, we discussed our results in context of electric modulus formalism. Basically the grain and the grain boundary effects can be divided into two different temperature regions, i.e., grain effects at low temperature (below 350 K), and grain boundary effects at high temperatures (above 350 K). Here well-resolved big semicircle was observed for L3 from grain effects at low temperature, which reduced with increase in the layers of MLNs. With increase in temperature, grain effect moved out partially, while grain boundaries effect entered in the measured frequency range. Both effects were observed for higher number of layers at elevated temperatures. This behavior is unlike the polycrystalline MLNs where grain and grain boundary effects were separated in two distinct temperature regions [19]. The magnitude of grain capacitance increased from L3 to L9 at low temperatures (<350 K) and the magnitude of grain boundary capacitance decreased from L3 to L9 at elevated temperatures.

The imaginary electrical modulus (M'') of L3, L5, and L9 MLNs thin films are shown in Fig. 6a–c, respectively, as a function of frequency at different temperatures. The relaxation frequency of grain and grain boundary capacitance almost fell into two different frequencies and temperature ranges matching well with impedance data. The peak position of the relaxation frequencies due to grain effect shifted rapidly toward higher frequency side with increase in temperature, while in case of grain boundary effect it is confined in low frequency window. Above ~400 K, the grain boundary peaks start appearing in the studied frequency window at the same time grain peaks moves out from the frequency window. It can be calculated from the modulus loss data that the difference in magnitude between C_g and C_{gb} decreases with increase in the number of layer of MLs, which indicates the increase of the inter-diffusion region between PZT and CFO with increasing number of layers resulting in more heterogeneous structure. The intensities of the grain peaks are nearly 14, 8, and 3–4 times greater than those from grain boundary. These results matched well with the results obtained from modulus complex plot. This indicates that the grain capacitance is about 14, 8, and 4 times smaller than that of the grain boundary. The difference between C_g and C_{gb} are higher compared to polycrystalline MLNs indicating less effects of grain boundary in highly oriented MLNs, which may be one of the reason to enhance polarization/dielectric properties for higher configurations (L9) [19, 25].

To explain the above results, we analyzed our data with complex electrical modulus formalism. The electric modulus, $M^*(\omega)$, corresponds to the relaxation of the electric field in the material when the electric field displacement remains constant. The expression for the decay of electric field in time domain can be written as:

$$E(t) = E(0) \times \phi(t), \tag{10}$$

where $\phi(t)$ is a macroscopic decay function of the general form

$$\phi(t) = \int_0^\alpha g(\tau) e^{(-t/\tau)\beta} \mathrm{d}\tau \tag{11}$$

where τ is an electric or conductivity relaxation time, and $g(\tau)$ is a normalized density function for relaxation times. In the frequency domain, this process may be described by

$$M^*(\omega) \equiv 1/\varepsilon^*(\omega) = M' + iM'', \tag{12}$$

$$M^*(\omega) = M_s \left[1 - \int_0^\alpha \exp(-i\omega t)\{-\mathrm{d}\phi(t)/\mathrm{d}t\}\mathrm{d}t \right], \tag{13}$$

$$= M_s \left[\int_0^\alpha g(\tau)[i\omega\tau/(1+i\omega\tau)]\mathrm{d}\tau \right], \tag{14}$$

where M_s is the high-frequency limit of the real part of the electrical modulus [35, 36].

The M'' fitting data for each multilayer structure were performed using the known Kohlraush–William–Watt (KWW) stretched exponential function [37, 38].

$\phi(t) = \phi_0 \exp\left[-(t/\tau)^\beta\right]$ is the decay function of the electric field within the material.

Where β is the stretched exponent parameter ($0 < \beta < 1$) and it characterizes width of the relaxation time distribution. τ is defined as the most probable relaxation time.

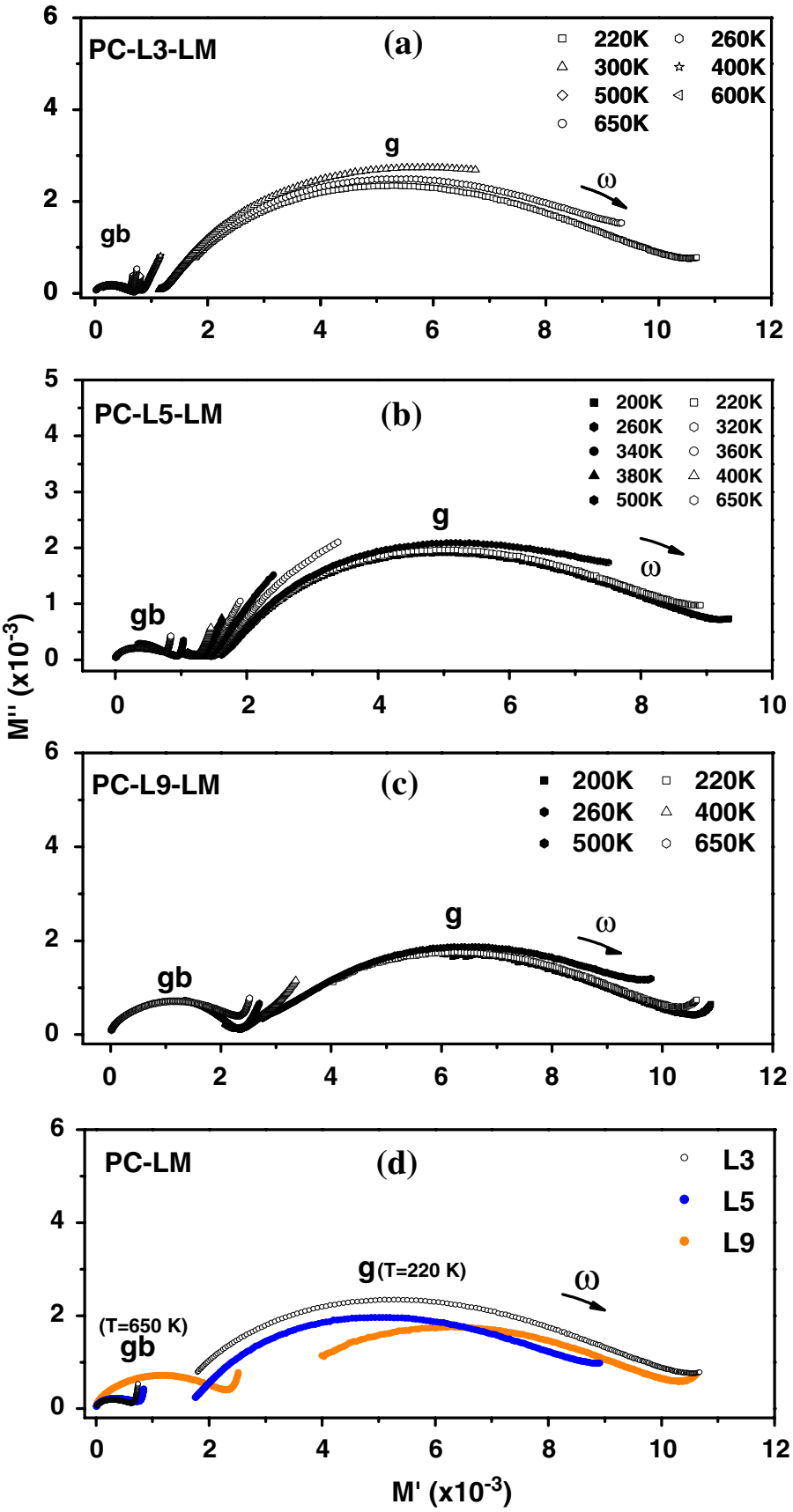

Fig. 5 **a–c** Complex electric modulus plane plot (M'' versus M') at different temperatures for L3, L5, and L9, PZT/CFO structures. **d** M'' versus M' plot for PZT/CFO-LSCO coated MgO (PC-LM) multilayer structures at 220 and 650 K

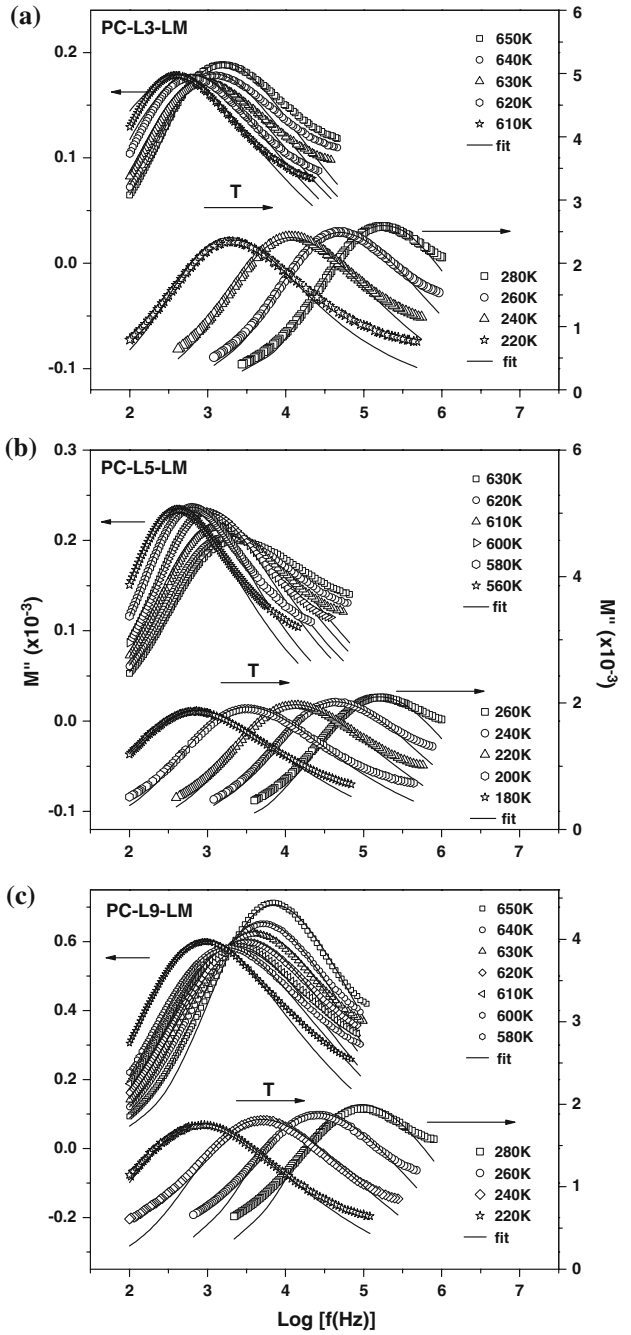

Fig. 6 Frequency dependence of imaginary part of electric modulus (M'') for **a** L3, **b** L5, and **c** L3 PZT/CFO MLN thin films, at low (lower) and higher (upper) temperatures, respectively

The modulus fitting for each multilayer structure was performed using the procedure of Moynihan et al. [39] by employing the fitting algorithm described elsewhere [40]. The continuous lines in Fig. 6a–c are the fitted values of M'', whereas the symbols correspond to the experimental data. The close agreement between the experimental data and the fitting curve is evident from Fig. 6a–c for L3, L5, and L9 multilayers films.

The stretched exponential parameters β obtained from the fitting were listed in Table 2. It was to be noted that β is independent of the temperature (i.e., the distribution of relaxation times is independent of temperature). For MLNs structures β_g and β_{gb} values are very close, this mean there is no significant difference in the width of the relaxation spectra in case of the grain and grain boundary relaxation process in two different temperature regions. It also suggests the distribution of relaxation time becoming similar with increasing number of layers. It is found that β increases with decreasing interactions among mobile carriers resulting in increase in conductivity [41, 42]. Our results show that β remains nearly constant with increase in number of layers in highly oriented MLNs strongly suggesting less contribution of grain boundary conductivity.

The relaxation time τ resulting from the M'' fits, for the low and high temperature relaxation peaks, were plotted against the inverse temperature. We found that the fitted τ value at different temperatures was follow by Arrhenius law. The activation energies of the grain and grain boundaries calculated from the slopes of the fitted straight lines are given in Table 2. The values corresponding to E_{gb} are in good agreement with values obtained from Z'' versus f plot $\left(E'_{gb}\right)$. The activation energy due to grain effect is almost similar for all the ML indicating response time decreases with identical rate. The value of E'_{gb} increases with increase in the layers of ML, indicating lowering the grain boundary capacitance, which matched well with the value calculated from the modulus loss spectra and observed in impedance loss spectra.

AC conductivity spectroscopy

Figure 7a shows the frequency dependence conductivity of MLNs at different temperatures. AC conductivity plots of all the MLNs showed frequency dispersion and merger of conductivity spectra at lower and higher frequencies, respectively, with the increase in temperature. In the experimental frequency window, the conductivity spectra can be easily distinguished in three conductivity regions above 400 K: (i) frequency independent conductivity in the low frequency region (<1 kHz), (ii) a frequency dependent plateau in the mid frequency region, and (iii) frequency dependent conductivity at high-frequency region. An enhancement of 3–4 orders of frequency independent conductivity were found with the increase in temperature (from 220 to 650 K), this behavior becomes almost similar for all MLNs.

Above observation in conductivity spectra of MLNs can be explained on the basis of the jump relaxation model (JRM) and conduction through grain boundaries. The frequency independent plateau at low frequencies for higher temperatures (>600 K) is attributed to the long-range

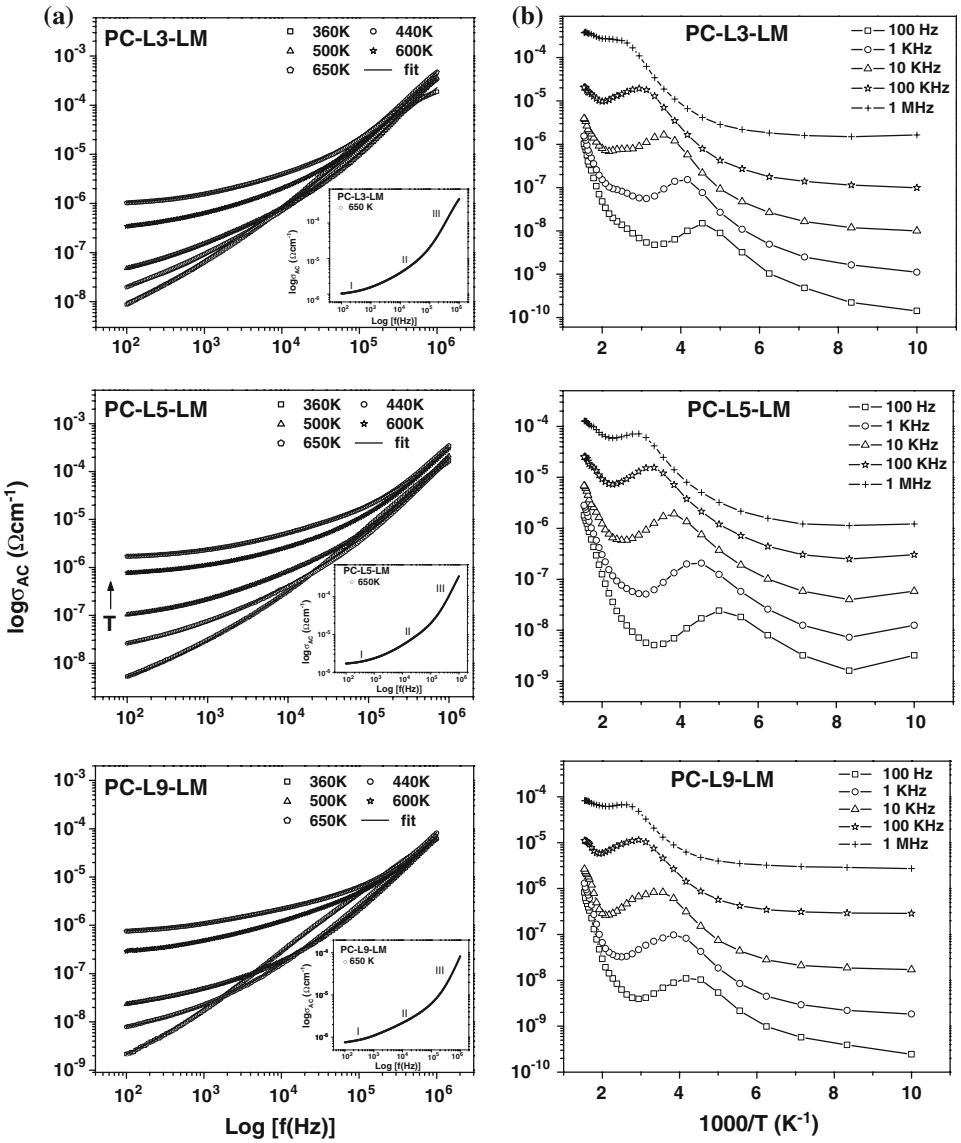

Fig. 7 **a** Frequency dependence plot of the AC conductivity at different temperatures, the double power law fits are shown as *continuous lines*; and **b** temperature dependence of the AC conductivity at different frequencies, for L3, L5, and L9 PZT–CFO MLN thin films

translational motion of ions contributing to DC conductivity σ_{DC}. The observed frequency independent DC conductivity was explained at higher temperatures by Funke [43] in the JRM. According to this model, the conductivity at low frequency region is associated with the successful hops to its neighborhood vacant site due to the available long time period; such successive jumps result in a long-range translational motion of ions contributing to DC conductivity. At high frequencies ($>10^4$ Hz), two competing relaxation processes may be visualized: (i) the jumping ion to jump back to its initial position (correlated forward–backward–forward), i.e., unsuccessful hopping and (ii) the neighborhood ions become relaxed with respect to the ion's position (the ions stay in the new site), i.e., successful hop. The increase in the ratio of successful to unsuccessful hopping results in a more dispersive conductivity at high frequencies. A convenient formalism to investigate the frequency behavior of conductivity at constant temperature in a variety of materials is based on the power relation proposed by Jonscher [44, 45]:

$$\sigma(\omega) = \sigma(0) + A\omega^n \tag{15}$$

where $\sigma(\omega)$ is the total conductivity, $\sigma(0)$ the frequency independent conductivity, and the coefficient A and exponent n ($0 < n_1 < 1$) are temperature and material intrinsic property dependent constants. The term $A\omega^n$ contains the AC dependence and characterizes all dispersion phenomena. The conductivity resulting in the present study does not follow above power relation. The insets of Fig. 7a clearly indicate a DC plateau (region I) at very low frequencies, and with increase in frequency, two dispersion regions appear; the low frequency dispersion is associated

with the grain boundary (large capacitance value) (region II) and the high-frequency one with grains (smaller capacitance value) (region III).

Applying the JRM, the frequency dependence of the conductivity of MLNs, the data have been fitted to the following double power law [43, 46] to describe the different contributions to conductivity;

$$\sigma(\omega) = \sigma(0) + A_1\omega^{n_1} + A_2\omega^{n_2} \quad (16)$$

which means that at very low frequencies, an almost frequency independent region is present, followed by two dispersive regions. The term $\sigma(0)$ (region I) corresponding to the translation hopping gives the long-range electrical transport (i.e., DC conductivity) in the long time limit. The second term $A_1\omega^{n_1}$, which was assigned to the region II, the exponent $0 < n_1 < 1$, characterizes the low frequency region and corresponds to the translational hopping motion (short-range hopping). Whereas, the one at high frequencies $A_2\omega^{n_2}$ is associated with the region III, the exponent $0 < n_2 < 2$ corresponds to a localized or reorientational hopping motion [44, 47]. The conductivity behavior of L3, L5, and L9 MLNs fitted with the double power law by nonlinear regression analysis is shown by solid lines in Fig. 7a at different temperatures.

Figure 7b shows the AC conductivity as a function of inverse temperature. It increases with temperature giving a "bumplike" graph between 200 and 380 K followed by Arrhenius character at elevated temperatures. The "bump" near 200–380 K corresponds to a step from high to low dielectric constant [25]. At high temperatures, all conductivity curves seem to be convergent. Such a conductive regime tends to the σ_{DC} component. In the high temperature side of Fig. 7b, the steep slope reflects the energy, which is required both to create and move defects [43]. At low temperature (<400 K), the σ_{DC} versus 1,000/T experienced a separation with the frequency and an increase in the magnitude of the AC conductivity is observed with increase in frequencies. It can be estimated from Fig. 7b, and this is a consequence of the fact that the required energy correlated with forward–backward hopping is only a fraction of the energy necessary to activate long-range diffusive conduction.

Polarization study

Figure 8a, b and insets show the temperature dependence of the ferroelectric polarization for L3, L5, L9 MLNs, and pure PZT grown under the same conditions, respectively. The well-defined and saturated ferroelectric hysteresis for all of the MLNs is obtained at room temperature as shown in Fig. 8a. As the temperature is decreased from 300 to 200 K, the hysteresis loop diminished with enhanced coercive field and became nearly zero at 100 K (Fig. 8b).

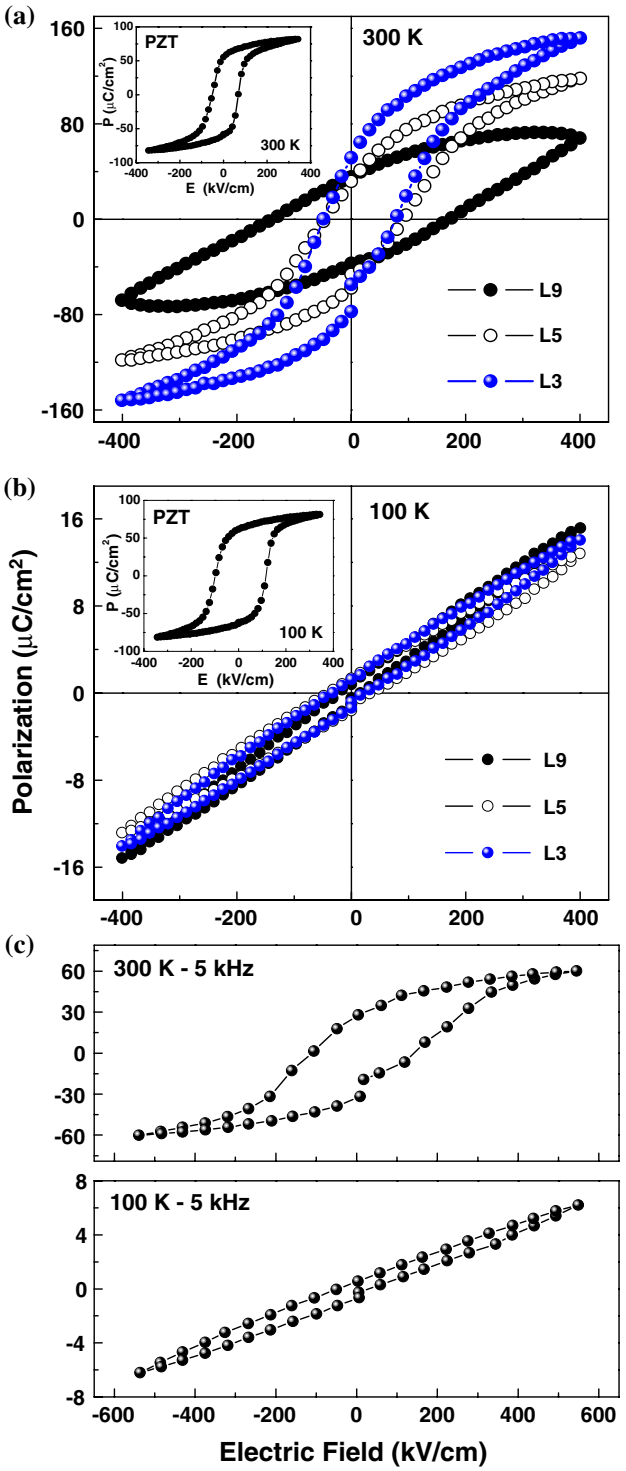

Fig. 8 Polarization versus applied electric field at **a** 300 K and **b** 100 K for high-oriented MLN thin films at 12 V. From the inset *P–E* loop for PZT thin films at the respective temperature. **c** Ferroelectric loop measure at 19 V, 5 kHz, at 300 and 100 K for PC-L3-LM thin film, grown on LSCO-coated (100) MgO substrate

These flop ferroelectric loops for all MLNs structures were recovered during heating. This process was completely reversible increasing the temperature. In order to check the

intrinsic behavior of the layered structure, these experiments were carried out several times on different substrates, each time we observed complete reversal of polarization. The reversibility of the process indicated that the decrease in the remanent polarization (P_r) with temperature was neither due to space charge effects nor due to the pinning of ferroelectric domains by defects or magnetic domains. For comparison, inset in Fig. 8a and b show the ferroelectric loop for pure PZT thin film grown under the same conditions at 100 and 300 K respectively, there was no distortion of the loop-shape with decrease in temperature, and an increase of only $\sim$20% in the coercive field was observed.

Then question arises, as to what is the role of the CFO layer in annihilation of the ferroelectric properties of the MLNs thin films at low temperature? Yang et al. [27] reported similar reduction of P_r with decrease in temperature for SBT films. They attributed this phenomenon to the progressive defect-induced pinning of the switchable polarization with reduction in temperature. The effect was considered to be an intrinsic in SBT thin films. In the present study, no reduction in P_r was observed in the pure PZT thin films when the temperature was lowered to 100 K from room temperature. For SBT films, the reduction of P_r with the lowering of temperature was attributed to enhance pinning of the switchable polarization by the point defects. This explanation could not hold for the MLNs system. In the present system, the reduction in P_r cannot be explained on the basis of the above observation because there is only a small amount of mixing of PZT and CFO at the interface without any other impure phase causing decrease in polarization significantly. The interior of PZT layer could not be pinned on lowering temperature by either point defects or magnetic domain situated at the grain boundaries and PZT–CFO interface.

Other possibilities to flop ferroelectric polarization are development of space charge near the interface of the layers of MLNs. In order to rule out the space charge effects, we performed the frequency dependent ferroelectric polarization study. Figure 8c shows the *P–E* curves of L3 MLNs at 300 and 100 K at 5 kHz, it behaves exactly the same as that of the previous observation for low frequency. The above two experiments suggest that the dynamic flop of polarization is not due to space charge effects and defect-induced pinning of the switchable polarization.

The flop of polarization at low temperature can be explained in the context of dynamic temperature–frequency dependent ME coupling. To investigate ME behavior, ferromagnetic properties (i.e., magnetic hysteresis (*M–H*)) were measured on the MLNs structures at different temperatures ranging from 4 to 400 K. Although the magnetization of the LSCO buffer layer was only 2–4% that the MLNs structure, we subtracted this value from the

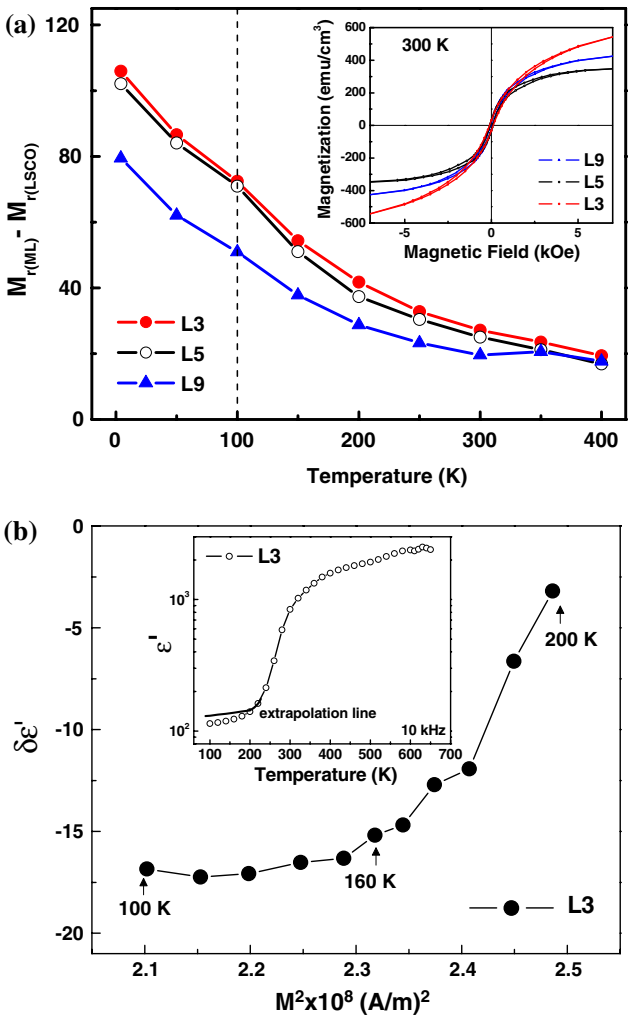

Fig. 9 **a** Temperature dependence of the remanent $(M_{r(ML)} - M_{r(LSCO)})$ magnetization and from the inset, the magnetic loop at 300 K, for L3, L5, and L9 multilayer structures. **b** The relation between $\delta\varepsilon$ and M^2 below critical temperature $T_c = 200$ K for L3 PZT/CFO MLN thin films. In the inset, the temperature dependence of the real part of the permittivity at 10 kHz and respective extrapolation from T_c is shown

magnetization value of MLs. The temperature variation of the remanent magnetization $\left(\Delta M_r = M_{r(ML)} - M_{r(LSCO)}\right)$ for L3, L5, and L9 MLNs structures are shown in Fig. 9a. Three order enhancements in ΔM_r values were observed when the temperatures decreased from 400 to 100 K. The reduction and annihilation (at 100 K) of the ferroelectric properties coincided with the improvements in the magnetization of the ML films, suggesting that dynamic ME coupling existed in the ML systems.

Dynamic magneto-electric coupling

Figure 9a shows remanent magnetization $(\Delta M_r = M_{r(ML)} - M_{r(LSCO)})$ of L3, L5, and L9 MLNs as a function of

temperature. The well-defined magnetic hysteresis loops were observed in all samples, with the presence of a long-range ordered magnetic structure as shown in the inset of Fig. 9a. We did not see any significant change in the magnetization curve; however, ΔM_r values were larger for L3 compared to L5 and L9. This could be attributed to the presence of magnetically "dead" layers between the CFO and PZT interfaces with increasing numbers of layers [48].

We have explained the dynamic temperature and frequency dependent ME coupling in light of the Ginzburg–Landau theory for the second-order phase transition of ferro-electromagnets, and it can be ascribed to the ME coupling term γP^2M^2 in the thermodynamic potential. The reduction in ferroelectric properties and improvements in the magnetic properties have been observed in $BiMnO_3$ and $PbFe_{1/2}Nb_{1/2}O_3$ multiferroic ME single crystal materials [49, 50]. Kimura et al. [49] and Yang et al. [50] observed kink in the dielectric constant (ε') near the Néel temperature (T_N) corresponding to the onset of ferromagnetic ordering, and a fairly large suppression of ε' around T_N with the application of the external magnetic field. In the present case, magnetic ordering increases with decrease in temperature (not at particular Néel temperature (T_N)), which in turn linearly changed the dielectric constant below 160 K as shown in Fig. 9b for L3 MLNs.

The thermodynamic potential, Φ, in a ferroelectromagnet can be written as:

$$\Phi = \Phi_0 + \alpha P^2 + \frac{\beta}{2}P^4 - PE + \alpha' M^2 + \frac{\beta'}{2}M^4 - MH + \gamma P^2 M^2 \quad (17)$$

where P and M are polarization and magnetization, respectively; and Φ, α, β, α', β', and γ are temperature dependent. The term γP^2M^2 in Eq. 17 corresponds to the exchange ME interaction, which gives rise to the deviation of the dielectric susceptibility, $\chi^E(T) = \partial\Phi^2/\partial P^2$. Below the critical temperature (T_c), the difference of $\chi^E(T)$ with the values obtained by extrapolation of itself from the critical temperature (T_c), where the polarization started deteriorating into the region $T < T_c$, was denoted as $\delta\chi^E$. Since $\delta\varepsilon' = 4\pi\delta\chi^E$, below T_c is proportional to the square of the magnetic order parameter:

$$\delta\varepsilon' \sim \gamma M^2 \quad (18)$$

The inset of Fig. 9b shows the temperature dependence of the real dielectric permittivity of L3 MLNs at 10 kHz. Below $T_c = 200$ K, the solid line corresponds to the deviation of ε' versus T from the values obtained by extrapolation. The magnetization (M) versus temperature (T) was obtained from ZFC curves under a magnetic field of 100 Oe (not shown). The relation of $\delta\varepsilon'$ as a function of M^2 is given in Fig. 9b for L3 MLNs structures. A linear behavior was observed between $\delta\varepsilon'$ and M^2 (i.e., $\delta\varepsilon \sim \gamma M^2$) below 150 K. These results led to the conclusion that the layered nanostructures had strong dynamic ME coupling attributable to the coupling term γP^2M^2 in the thermodynamic potential.

Fatigue properties

The fatigue was tested for all MLNs at 1 kHz square pulses (to eliminate the space charge effects) and amplitude of 250–350 kV/cm for device applications. Figure 10 shows the remanent polarization as a function of switching cycles for all MLNs. All multilayers illustrated good fatigue properties; the percentage of decay of switching polarization in MLNs films was about 0–20% at 10^8 switching cycles. The degradation of the remanent polarization resembles with the polarization fatigue of PZT films on Pt electrodes mainly originates from the accumulation of the oxygen vacancies and domain wall pinning near the electrode interfaces [51–53]. Ramesh et al. showed that the problem of fatigue can be reduced by using oxide electrodes, such as RuO_2, LSCO, or $SrRuO_3$ [54, 55], which act as sources for maintaining the oxygen ions. This indicates that maintaining the oxygen ions in the material matrix prevents the degradation of ferroelectric polarization in MLNs thin films. We believe that in the case of MLNs thin films, even with dissimilar bottom (LSCO) and top (Pt) electrodes, the very low degradation of the P_r value results from the feeding of oxygen ions to the intermediate PZT layers from the bottom LSCO layer and CFO intermediate layers. The perovskite oxide layers can provide a net "pool" to compensate for the charge accumulation near the interfaces [56].

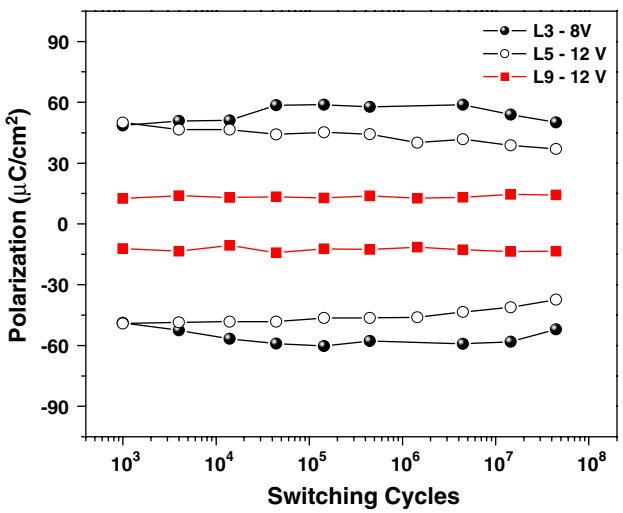

Fig. 10 Ferroelectric fatigue L3, L5, and L9 MLN structures

Conclusions

The present paper investigates the design and characterization of PZT/CFO MLNs. The different configurations L3, L5, and L9 MLNs were fabricated on LSCO-coated MgO substrate using pulsed laser deposition. All of the configurations showed highly oriented along (100), the pure phase of parent layers, little inter-diffusions near the interfaces, and uniform distribution of layers over several micron, these micro-structural properties were characterized by XRD, Raman spectroscopy, and TEM. A great deal of strain was found across the in-plane and out of plane between the parent layers, which may cause electro-strictions along the interface and coupled magnetic and electric properties. The temperature and frequency dependent dielectric properties showed mainly bulk permittivity contributions and extrinsic contributions below and above 400 K, respectively. The Cole–Cole plots and the imaginary part of the permittivity as a function of frequency indicate marked deviation from the ideal Debye-type relaxation and it is poly dispersive in nature above room temperature whereas these MLNs obey very nearly to the Debye-type relaxation at low temperature. The impedance spectroscopy results indicate weak grain effects and grain boundary effects (well-resolved semi-circles) at low temperatures and elevated temperatures, respectively. The electric modulus illustrated excellent grain and grain boundary capacitance behavior in two temperature windows, the magnitude of the grain capacitance are nearly 14, 8, and 3–4 times greater than those from the grain boundary. The frequency dependent conductivity suggests three types of conduction processes in MLNs, i.e., (i) frequency independent conductivity in low frequency region (<1 kHz), (ii) a frequency dependent plateau in mid frequency region, and (iii) frequency dependent conductivity at high-frequency region. The magnitude of the frequency independent conductivity increases with enhancement of temperature. The temperature dependent ferroelectric polarization gradually decreased with decrease in temperature, whereas complete flop of polarization was observed at 100 K, and a similar behavior was observed for different frequencies for all MLNs configurations. The three-fold enhancements in remanant magnetization were seen from 300 to 100 K with higher rate of enhancement below 160 to 100 K, which may play vital role in degradation of dielectric constant and ferroelectric polarization. A thermodynamical Ginzburg–Landau theory for the second-order phase transition was used to analyze the linear ME coupling, the change in dielectric constant slope linearly obey the relation $\delta\varepsilon \sim \gamma M^2$, where M represents the magnetization at ZFC suggesting the dynamic temperature dependent ME coupling. The fatigue test for all the MLNs displayed 5–20% degradation of ferroelectric polarization at room temperature suggesting that potential candidate for multiferroic ME memory applications.

Acknowledgements This work was supported in parts by DOE DE-FG02-08ER46526, DoD-HIS W911NF-06-1-0030 and DEPSCoR W911NF-06-1-0183 grants. One of us (N. Ortega) was supported by a NSF-IFN-EPSCOR Fellowship.

References

1. Scott JF (2007) Science 315:954
2. Spaldin NA, Fiebig M (2005) Science 309:391
3. Eerenstein W, Mathur ND, Scott JF (2006) Nature 442:759
4. Spaldin NA, Pickett WE (2003) J Solid State Chem 176:615
5. Wang J, Neaton JB, Zheng H, Nagarajan V, Ogale SB, Liu B, Viehland D, Vaithyanathan V, Schlom DG, Waghmare UV, Spaldin NA, Rabe KM, Wuttig M, Ramesh R (2003) Science 299(14):1719
6. Ramesh R, Spaldin NA (2007) Nature 6:21
7. Zheng H, Wang J, Loand SE, Ma Z, Mohaddes-Ardabili L, Zhao T, Salamanca-Riba L, Shinde SR, Ogale SB, Bai F, Viehland D, Jia Y, Schlom DG, Wuttig M, Roytburd A, Ramesh R (2004) Science 303:661
8. Petrov VM, Srinivasan G, Laletsin U, Bichurin MI, Tuskov DS, Paddubnaya N (2007) Phys Rev B 75:174422
9. Srinivasan G, Rasmussen ET, Gallegos J, Srinivasan R, Bokhan YI, Laletin VM (2001) Phys Rev B 64:214408
10. Dong S, Li J-F, Viehland D (2006) J Mater Sci 41:97. doi: 10.1007/s10853-005-5930-8
11. Zhang JX, Dai JY, Lu W, Chan WHL (2009) J Mater Sci. doi: 10.1007/s10853-009-3512-x
12. Duan Ch-G, Jaswal SS, Tsymbal EY (2006) Phys Rev Lett 97:047201
13. Niranjan M-K, Velev JP, Duan Ch-G, Jaswal SS, Tsymbal EY (2008) Phys Rev B 78:104405
14. Zhou JP, He H, Shi Z, Nan CW (2006) Appl Phys Lett 88:013111
15. Murugavel P, Singh MP, Prellier W, Mercey B, Simon Ch, Raveau B (2005) J Appl Phys 97:103914
16. Ortega N, Bhattacharya P, Katiyar RS, Dutta P, Manivannan A, Seehra MS, Takeuchi I, Majumder SB (2006) J Appl Phys 100:126105
17. Raymond O, Font R, Suarez-Almodovar N, Portelles J, Siqueiros JM (2005) J Appl Phys 97:084108
18. Srinivas K, Sarah P, Suryanarayana SV (2003) Bull Mater Sci 26:2–274
19. Ortega N, Kumar A, Bhattacharya P, Majumder SB, Katiyar RS (2008) Phy Rev B 77:014111
20. Liu J, Duan Ch-G, Mei WN, Smith RW, Hardy JR (2005) J Appl Phys 98:093703
21. Ni WQ, Zheng XH, Yu JC (2007) J Mater Sci 42:1037. doi: 10.1007/s10853-006-1431-7
22. Catalan G (2006) Appl Phys Lett 88:102902
23. Catalan G, Scott JF (2007) Nature 448:E4. doi:10.1038/nature 06156
24. Catalan G, O'Neill D, Bowman RM, Gregg JM (2000) Appl Phys Lett 77:3078
25. Ortega N, Kumar A, Katiyar RS, Scott JF (2007) Appl Phys Lett 91:102902
26. Sinclair DC, Adams TB, Morrison FD, West AR (2002) Appl Phys Lett 80:2153
27. Yang P, Carroll DL, Robert JB, Schwartz W (2002) Appl Phys Lett 81:4583
28. Bousquet E, Dawber M, Stucki N, Lichtensteiger C, Hermet P, Gariglio S, Triscone J-M, Ghosez P (2008) Nature 452:732

29. Kundys B, Simon Ch, Martin Ch (2008) Phys Rev B 77:172402
30. Cole KS, Cole RH (1941) J Chem Phys 9:341
31. Schmidt R, Eerenstein W, Winiecki T, Morrison FD, Midgley PA (2007) Phys Rev B 75:245111
32. Jiang AQ, Scott JF, Dawber M, Wang C (2002) J Appl Phys 92:6756
33. Liu J, Duan Ch-G, Yin W-G, Mei WN, Smith RW, Hardy JR (2004) Phys Rev B 70:144106
34. Victor P, Bhattacharyya S, Krupanidhy SB (2003) J Appl Phys 94:5135
35. Macedo PB, Moynihan CT, Bose R (1972) Phys Chem Glasses 13:171
36. Provenzano V, Boesch LP, Volterra V, Macedo PB, Moynihan CT (1972) J Am Ceram Soc 55:492
37. Kohlrausch R (1847) Ann Phys. (Leipzig) 12:393
38. Williams G, Watts DC (1970) Trans Faraday Soc 66:80
39. Moynihan CT, Boesch LP, Laberge NL (1973) Phys Chem Glasses 14:122
40. Baskaran N (2002) J Appl Phys 92:825
41. Patel HK, Martin SW (1992) Phys Rev B 45:10292
42. Ngai KL, Greaves GN, Moynihan CT (1998) Phys Rev Lett 80:1018
43. Funke K (1993) Prog Solid State Chem 22:111
44. Jonscher AK (1977) Nature 264:673
45. Murugaraj R (2007) J Mater Sci 42:10065. doi:10.1007/s10853-007-2052-5
46. Almond AP, West AR, Grant RJ (1982) Solid State Commun 44:277
47. Pelaiz-Barramco A, Gutierrez-Amador MP, Huanosta A, Valenzuela R (1998) Appl Phys Lett 73:2039
48. Calderon MJ, Brey L, Guinea F (1999) Phys Rev B 60:6698
49. Kimura T, Kawamoto S, Yamada I, Azuma M, Takano M, Tokura Y (2003) Phys Rev B 67:180401 (R)
50. Yang Y, Liu JM, Huang HB, Zou WQ, Bao P, Liu ZG (2004) Phys Rev B 70:132101
51. Al-Shareef HN, Kingon AI, Chen X, Bellur KR, Auciello O (1994) J Mater Res 9:2968
52. Yoo IK, Desu SB (1992) Mater Sci Eng B 13:319
53. Warren WL, Dimos D, Tuttle BA, Nasby RD, Pike GE (1994) Appl Phys Lett 65:1018
54. Ramesh R, Chan WK, Wilkens B, Gilchrist H, Sands T, Tarascon JM, Keramidas VG, Fork DK, Lee J, Safari A (1992) Appl Phys Lett 61:1537
55. Dat R, Lichtenwalner DJ, Auciello O, Kingon AI (1994) Appl Phys Lett 64:2673
56. Bao D, Wakiya N, Shinozaki K, Mizutani N (2002) J Phys D Appl Phys 35:L1